Available online at www.sciencedirect.com

SciVerse ScienceDirect

Procedia Computer Science 9 (2012) 822 – 831

Procedia Computer Science

www.elsevier.com/locate/procedia

International Conference on Computational Science, ICCS 2012

Numerical Optimization and Experimental Validation of a Low-Speed Wind Tunnel Contraction

Leifur Leifsson,[a,b*] Slawomir Koziel,[a] Fannar Andrason,[b] Kristjan Magnusson,[b] Armann Gylfason[c]

[a]*Engineering Optimization & Modeling Center, School of Science and Engineering, Reykjavik University, Menntavegur 1, 101 Reykjavik, Iceland*
[b]*CADIA/Laboratory for Unmanned Vehicles, Reykjavik University, Menntavegur 1, 101 Reykjavik, Iceland*
[c]*School of Science and Engineering, Reykjavik University, Menntavegur 1, 101 Reykjavik, Iceland*

Abstract

A low-speed wind tunnel is developed for fluid dynamics research at Reykjavik University. The tunnel is designed for conducting research on the flow past micro air vehicles, as well as fundamental research on turbulence. High flow quality is elemental for both research projects. The tunnel is of open suction type and is composed of a square inlet with a honeycomb and turbulence screens, settling chamber, contraction, experimental section housing, diffuser, and axial fan. Here, we describe the details of the design optimization procedure of the contraction, which is a key to getting a high quality flow in the experimental section. A high-fidelity computational fluid dynamic (CFD) flow solver is used to capture the nonlinear flow physics. Due to the high computational cost of the CFD simulations, surrogate-based optimization (SBO) is used to accelerate the design process. The SBO approach replaces direct optimization of the high-fidelity (accurate but computationally expensive) model by iterative optimization of a properly corrected low-fidelity model obtained from low-fidelity CFD simulations. The optimum contraction design is verified using high-fidelity CFD simulation, as well as by experimental measurements.

Keywords: Wind tunnel design; contraction shape optimization; SBO; CFD; experimental validation.

1. Introduction

A low-speed wind tunnel, intended for fluid dynamics research, is under development at the author's institution. The utilization of the facility will be twofold; involving the research on micro air vehicles (MAVs), both with fixed- and flapping-wings, as well as fundamental research on turbulence. High flow quality is essential for both these research projects. The facility is expected to provide capability for the characterization of the aerodynamic performance of MAVs at low Reynolds numbers (Re < 100,000). The required flow speed range is from 0 to 30 m/s. The work conducted in the tunnel will involve analysis of various aspects of MAVs, such as the wing shape and flapping parameters, and control effectiveness.

The wind tunnel will be of open suction type, as shown in Fig. 1, and is composed of a square inlet with a honeycomb and turbulence screens, settling chamber, contraction, experimental section housing, diffuser, and axial

* Corresponding author. Tel.: +354-599-6379 ; Fax: +354-599-6201; *E-mail address*: leifurth@ru.is

doi:10.1016/j.procs.2012.04.088

fan. The experimental section is located in a large enclosure which houses the experimental equipment (the MAV) and the instrumentation (such as a force balance and a particle image velocimetry (PIV) system).

The contraction is a critical component of the wind tunnel for the provision of high quality test flow in the working section [1]. The shape of the contraction controls the quality (such as flow angularity and uniformity, as well as turbulence intensity) of the flow at the outlet. As the effects of the shape on the flow are quite complicated, it is necessary to use computational fluid dynamics (CFD) to make the design decisions, such as the length, contraction ratio, and the wall shape. The process can be automated using a numerical optimization procedure. Example of such work can be found in work by Watmuff [2], Su [3], Doolan and Morgans [4], and Mathew et al. [5]. Due to the computational expense of three-dimensional high-fidelity CFD simulations, and the fact that numerical optimization requires a large number of function calls, all of aforementioned work use traditional fluid flow solvers (coupled potential and viscous fluid flow solvers), which are computationally cheap, and traditional optimization techniques. The final design is then typically verified by using a high-fidelity flow solver.

The objective of this work is to design the shape of the contraction so that the flow in the experimental section is of high quality. To be able to capture nonlinear flow physics and geometry of the problem accurately throughout the optimization process, the use of high-fidelity CFD simulation is necessary. The coupled potential and viscous flow solvers, as used in previous work [2-5], will not capture these effects accurately enough. As a matter of fact, high-fidelity simulations are essential. As demonstrated in Section 2, the contraction design obtained based on low-fidelity CFD analyses does not ensure the high-quality flow.

The use of high-fidelity CFD simulations comes at a high computational cost, which becomes prohibitive when using traditional gradient-based or population-based optimization schemes. Surrogate-based optimization (SBO) replaces direct optimization of the high-fidelity (accurate but computationally expensive) model by iterative optimization of a properly corrected low-fidelity model. This reduces the number of evaluations of the high-fidelity model and accelerates the optimization process.

In this work, we describe the design of the wind tunnel contraction using high-fidelity CFD simulation and SBO. In particular, we adopt the multi-fidelity approach with the high-fidelity model based on the steady Reynolds-averaged Navier-Stokes (RANS) equations, and the low-fidelity model based on the same equations, but with coarse discretization and relaxed convergence criteria. We use a simple response correction technique to create a surrogate that is subsequently used as a prediction tool to yield an approximate high-fidelity model optimum. On completion of the contraction design optimization, the entire wind tunnel was fabricated and assembled. Physical measurements of the flow quality in the experimental section have been performed to validate the final wind tunnel design. In particular, we mapped the flow speed within the cross-section of the experimental test section. The experimental results and comparisons with our computational model are presented.

2. Numerical Shape Optimization

This section presents the numerical shape optimization of the wind tunnel contraction. In particular, we present the problem formulation, the CFD model, the optimization methodology, and several design studies.

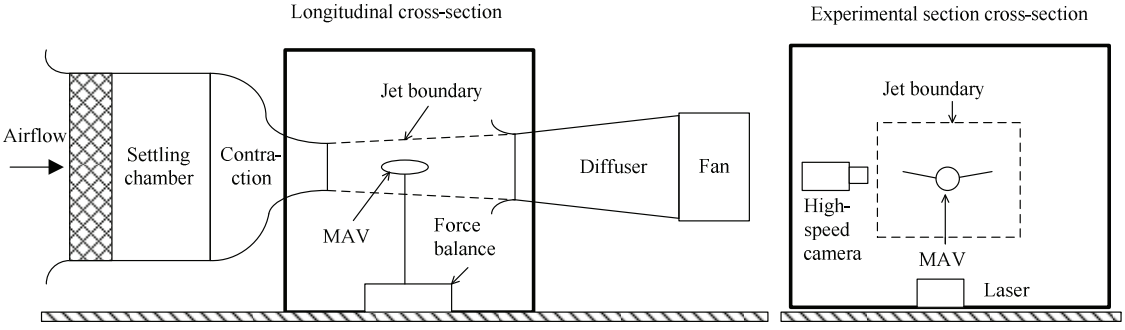

Fig. 1. A schematic of the wind-tunnel from the side, as well as a cross-sectional view of the test section.

2.1. Problem Formulation

A sketch of a typical square three-dimensional contraction shape is shown in Figs. 2a and 2b. At the outlet, the flow has to be uniform, and the boundary-layer needs to be thin to maximize the usable cross-sectional area. The overall goal is thus to maximize the flow uniformity at the outlet in terms of speed and angularity. More specifically, we want to minimize the variation of the speed (v) and angularity (α) at the horizontal and diagonal control directions in the outlet plane (Fig. 2c). The vertical control direction is not needed due to symmetry.

The variables controlling the contraction shape are the inlet size, the contraction area ratio, the length, and the wall shape. To simplify our problem, we will fix the inlet size, the contraction area ratio, and length. This is necessary in this particular work, since the size of the laboratory that houses the wind tunnel is a limiting factor. Given these parameters, the design variables are the parameters controlling the wall shape.

The contraction wall shape is defined by Bézier curves on the symmetry planes. The Bézier curves, of order n, are defined as (see, e.g., [6])

$$B(t) = \sum_{k=1}^{m} \sum_{i=0}^{n} \frac{n!}{i!(n-i)!} (1-t(k))^{n-i} t(k)^{i} P(i) \tag{1}$$

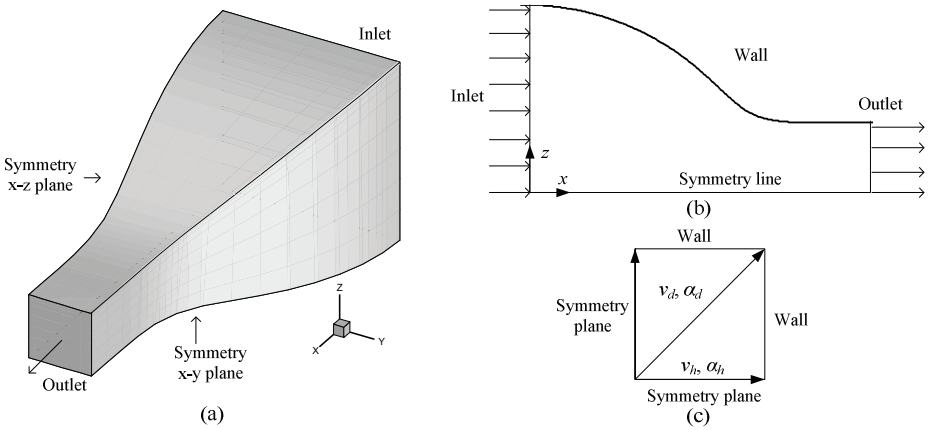

Fig. 2. (a) One fourth of a three-dimensional contraction shape; (b) view of the upper half of the x-z symmetry plane; (c) control directions in the outlet plane.

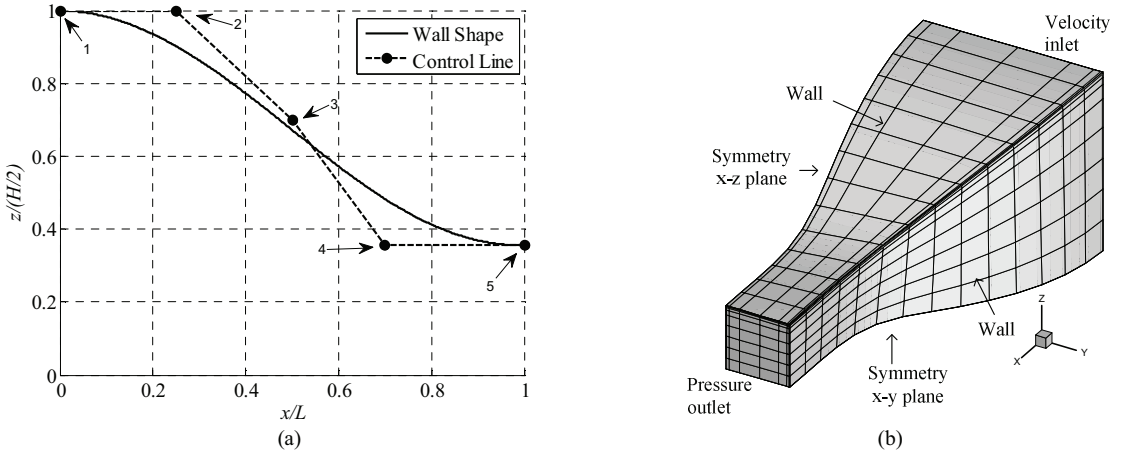

Fig. 3. (a) Bézier curve of the contraction wall shape (solid line) in the symmetry plane, and the control line (dashed line) with 5 control points (dots); (b) Example computational mesh of the three-dimensional contraction.

where $P(i)$, $i = 0,1,\ldots n$, are the control points, and t is an $1 \times m$ array with entries from 0 to 1. Any number of control points can be used to represent the wall shape. Here, we use 5 control points as shown in Fig. 3a. The first control point is fixed to the inlet height H. Control points 2 and 4 are fixed in the horizontal direction. The third control point is free. The fifth control point is fixed to the outlet height. In total, this gives 4 design variables. The design variable vector is written as $\boldsymbol{x} = [x_2\ x_3\ z_3\ x_4]^T$, where x and z are the coordinates of the corresponding control points.

2.2. Computational Fluid Dynamic Model

The flow is assumed to be steady, incompressible, and viscous. The steady Reynolds-averaged Navier-Stokes (RANS) equations are taken to be the governing flow equations for the high-fidelity CFD model with the k-ω SST turbulence model by Menter [7]. Due to symmetrical reasons, the computational domain is only one quarter of the contraction. The computational mesh is structured with brick elements and is generated using the computer code ICEM CFD [8]. The grid is made denser in the wall region. An example mesh is shown in Fig. 3b, along with the boundary conditions. A grid convergence study was performed to determine the appropriate mesh density. Initially, a relatively fine grid was developed and then the grid density was changed (the number of grid points halved or doubled) in several steps to observe the changes in the velocity field at the outlet. The fine mesh, used in the high-fidelity CFD model, has 50 elements in the x-direction, and 80 elements in the y- and z-directions. The total number of mesh cells is 320,000. The non-dimensional normal distance (y^+) from the wall to the first grid point is roughly one.

The numerical simulations are performed using the computer code FLUENT [9]. The flow solver is of implicit density-based formulation and the fluxes are calculated by an upwind-biased second-order spatially accurate Roe flux scheme. Asymptotic convergence to a steady state solution is obtained for each case. The iterative convergence of each solution is examined by monitoring the overall residual, which is the sum (over all the cells in the computational domain) of the L^2 norm of all the governing equations solved in each cell. The convergence criteria used in this work for the high-fidelity CFD model is the one that occurs first of the following: a maximum residual of 10^{-6}, or a maximum number of iterations of 1000.

The low-fidelity model is based on the same CFD model as the high-fidelity one. However, as the low-fidelity model will be used in place of the high-fidelity model in the optimization process, it needs to be faster in order to reduce the computational cost of the design process. The simulation time can be substantially reduced by making the grid coarser. Here, we used the medium mesh obtained from the grid convergence study. This mesh has 20 elements in the x-direction, and 40 elements in the y- and z-directions, with a total number of mesh cells of 32,000. The distance to the first nodal point was kept fixed. The simulation time is reduced further by reducing the number of iterations. We, therefore, relax the convergence criteria for the low-fidelity model by setting the maximum number of iterations to 15. The ratio of simulation time of the high-fidelity model to the low-fidelity model is around 250.

2.3. Optimization Methodology

In this section, we describe our approach to optimizing the contraction shape. As explained in Section 2.1, the goal is to obtain as uniform velocity field v as possible, where v is a function of four shape parameters $\boldsymbol{x} = [x_2\ x_3\ z_3\ x_4]^T$. In the following, we describe the formulation of the objective function, the surrogate-based optimization approach that is adopted here to design the contraction shape, as well as the construction of the surrogate model which is based on the low-fidelity CFD simulations.

We are interested in minimizing the variation of the velocity magnitude, i.e., the speed, as well as the velocity angle for the two control directions, horizontal and diagonal, denoted as $v_{h.f}(\boldsymbol{x},t)$, $\alpha_{h.f}(\boldsymbol{x},t)$, $v_{d.f}(\boldsymbol{x},t)$, $\alpha_{d.f}(\boldsymbol{x},t)$, with $0 \le t \le 1$ (0 corresponds to the contraction center, 1 corresponds to the wall). The subscript "f" indicates that the models are associated with high-fidelity CFD simulations. For the horizontal direction we are interested in minimizing $v_{h.f}(\boldsymbol{x},t)$ and $\alpha_{h.f}(\boldsymbol{x},t)$ for $0 \le t \le 0.9$, for the diagonal direction we want to minimize $v_{d.f}(\boldsymbol{x},t)$ and $\alpha_{d.f}(\boldsymbol{x},t)$ for $0 \le t \le 0.85$. Because our two objectives (velocity magnitude and angle) are non-commensurable, only one of them (angle) is treated directly, the other one (magnitude) is handled through penalty function. The objective function is therefore defined as

$$H_f(\boldsymbol{x}) = \max\{\Delta\alpha_{h.f}(\boldsymbol{x}), \Delta\alpha_{d.f}(\boldsymbol{x})\} + \beta\left[(\max\{\Delta v_{h.f}(\boldsymbol{x})/v_{h.f.\max}, \Delta v_{d.f}(\boldsymbol{x})/v_{d.f.\max}\} - \Delta v_{\max})/\Delta v_{\max}\right]^2, \quad (2)$$

where $\Delta v_{h.f}(\boldsymbol{x}) = \max\{0 \le t \le 0.9: |v_{h.f}(\boldsymbol{x},t)|\} - \min\{0 \le t \le 0.9: |v_{h.f}(\boldsymbol{x},t)|\}$, $\Delta v_{d.f}(\boldsymbol{x}) = \max\{0 \le t \le 0.85: |v_{d.f}(\boldsymbol{x},t)|\} - \min\{0 \le t \le 0.85: |v_{d.f}(\boldsymbol{x},t)|\}$, $v_{h.f.\max} = \max\{0 \le t \le 0.9: |v_{h.f}(\boldsymbol{x},t)|\}$, $v_{d.f.\max} = \max\{0 \le t \le 0.85: |v_{d.f}(\boldsymbol{x},t)|\}$. The definitions of $\Delta\alpha_{h.f}(\boldsymbol{x})$ and $\Delta\alpha_{d.f}(\boldsymbol{x})$ are similar. In our numerical experiments we use $\beta = 1000$. $\Delta v_{\max}$ is the maximum allowable variation of the velocity magnitude. Here, we set $\Delta v_{\max} = 0.01$.

In order to reduce the design cost, we exploit surrogate-based optimization (SBO) principle [10,11]. More specifically, the direct minimization of the high-fidelity objective function (2) is replaced by an iterative procedure [11],

$$\boldsymbol{x}^{(i+1)} = \arg\min_{\boldsymbol{x}} H_s^{(i)}(\boldsymbol{x}), \tag{3}$$

that generates a sequence of approximate solutions $\boldsymbol{x}^{(i)}$, $i = 0, 1, \ldots$, to the original problem $\operatorname{argmin}\{\boldsymbol{x} : H_f(\boldsymbol{x})\}$. Each $\boldsymbol{x}^{(i+1)}$ is the optimal design of the surrogate model $H_s^{(i)}$, $i = 0, 1, \ldots$. $H_s^{(i)}$ is assumed to be a computationally cheap and sufficiently reliable representation of H_f, particularly in the neighborhood of $\boldsymbol{x}^{(i)}$. Under these assumptions, the algorithm (3) is likely to produce a sequence of designs that quickly approach $\boldsymbol{x}_f^*$. Usually, the high-fidelity model is only evaluated once per iteration (at every new design $\boldsymbol{x}^{(i+1)}$) for verification purposes and to obtain the data necessary to update the surrogate model. Because of the low computational cost of the surrogate model, the cost of each iteration of the algorithm (3) is substantially lower than the cost of solving the original problem with the high-fidelity objective function. Moreover, the number of iterations for a well performing surrogate-based algorithm is substantially smaller than for any direct optimization method (e.g., gradient-based or pattern-search), which results in substantial time savings. In this work, the surrogate model is optimized using the pattern search algorithm [12].

The surrogate model $H_s^{(i)}$ is defined as

$$H_s^{(i)}(\boldsymbol{x}) = \max\{\Delta\alpha_{h.s}^{(i)}(\boldsymbol{x}), \Delta\alpha_{d.s}^{(i)}(\boldsymbol{x})\} + \beta\left[(\max\{\Delta v_{h.s}^{(i)}(\boldsymbol{x}), \Delta v_{d.s}^{(i)}(\boldsymbol{x})\} - dv_{\max})/dv_{\max}\right]^2, \tag{4}$$

where the definitions of $\Delta v_{h.s}^{(i)}(\boldsymbol{x})$, $\Delta v_{d.s}^{(i)}(\boldsymbol{x})$, $\Delta\alpha_{h.f}^{(i)}(\mathrm{x})$, and $\Delta\alpha_{d.f}^{(i)}(\boldsymbol{x})$ are based on the surrogate functions $v_{h.s}^{(i)}(\boldsymbol{x},t)$, $v_{d.s}^{(i)}(\boldsymbol{x},t)$, $\alpha_{h.s}^{(i)}(\boldsymbol{x},t)$, and $\alpha_{d.s}^{(i)}(\boldsymbol{x},t)$, and analogous to that for the high-fidelity model.

The surrogate functions can be constructed either from sampled high-fidelity model data using an appropriate approximation technique [13], or by utilizing a physically-based low-fidelity model [10]. Here, we exploit the latter approach as we have a reliable low-fidelity model at our disposal (see Section 2.2). Also, good physically-based surrogates can be constructed using a fraction of high-fidelity model data necessary to build accurate approximation models [14].

There are several methods of constructing the surrogate from a physically-based low-fidelity model. They include, among others, space mapping (SM) [10], various response correction techniques [15], manifold mapping [16], and shape-preserving response prediction [17]. Here, the surrogate model is created using a simple multiplicative response correction, which turns out to be sufficient for our purposes. An advantage of such an approach is that the surrogate is constructed using a single high-fidelity model evaluation, and it is very easy to implement.

At iteration i, the surrogate $v_{h.s}^{(i)}(\boldsymbol{x},t)$ of the velocity magnitude $v_{h.f}(\boldsymbol{x},t)$ is constructed using the multiplicative response correction of the form

$$v_{h.s}^{(i)}(\boldsymbol{x},t) = v_{h.c}(\boldsymbol{x},t)\frac{v_{h.f}(\boldsymbol{x}^{(i)},t)}{v_{h.c}(\boldsymbol{x}^{(i)},t)}, \tag{5}$$

where $v_{h.c}(\boldsymbol{x},t)$ is the low-fidelity velocity magnitude function. Similar definition holds for the remaining surrogate functions $v_{d.s}^{(i)}(\boldsymbol{x},t)$, $\alpha_{h.s}^{(i)}(\boldsymbol{x},t)$, and $\alpha_{d.s}^{(i)}(\boldsymbol{x},t)$. Note that the formulation (5) ensures zero-order consistency [18] between the surrogate and the high-fidelity model, i.e., $v_{h.s}^{(i)}(\boldsymbol{x}^{(i)},t) = v_{h.f}(\boldsymbol{x}^{(i)},t)$. While—in principle—this is not sufficient to ensure the convergence of the algorithm (2) to an optimum of the high-fidelity model, as demonstrated in Section 2.4, the algorithm performs very well. The primary reason is that the low-fidelity model is physically-based so that the changes of $v_{h.f}(\boldsymbol{x},t)$ and $v_{h.c}(\boldsymbol{x},t)$ are correlated under the change of the shape parameters $\boldsymbol{x}$. Figure 4 illustrates the surrogate model construction.

2.4. Results

The wind tunnel contraction shape has been optimized using the methodology described in Section 2.3. The contraction length was set to 2 m, the inlet width was set to 2 m, whereas the contraction area ratio is 8:1. For comparison and verification, we carried out four optimization runs using: (1) direct optimization of the low-fidelity model, (2) direct optimization of the high-fidelity model, (3) surrogate-based optimization using the methodology of Section 2.3, (4) surrogate-based optimization using the methodology of Section 2.3 embedded in the trust-region framework [19]. In all cases, the optimization engine was a pattern search algorithm [12]. The numerical results are presented in Table 1.

The results show that the shape obtained by optimizing the low-fidelity model does not bring much of the improvement in terms of reducing the velocity angle variation. As shown in Fig. 5, the corresponding contraction shape is actually quite similar to the initial one. This indicates that simply replacing the high-fidelity model by the low-fidelity one in the design process is not a good option. Direct optimization of the high-fidelity model substantially reduces $\Delta\alpha$ (from 4.6 to 1.6 degree), however, the design cost is quite substantial, 134 high-fidelity model evaluations. The surrogate based optimization enhanced by the trust-region framework yields the design with slightly worse reduction of $\Delta\alpha$ (2.0 degree), however, the design cost is much lower – only 13 equivalent high-fidelity model evaluations.

The surrogate-based optimization working without trust region yields much better design with respect to the velocity angle variation, $\Delta\alpha$ of only 0.7 degree and at a very low cost of less than 6 equivalent high-fidelity model evaluations. However, the Δv constraint is slightly violated in this case, which is a result of not using the trust-region approach (TR enforces satisfaction of Δv constraint in Case 3). The contraction shapes obtained in Cases 2 through 4 are rather similar to each other. Note that the lowest value of $\Delta\alpha$ corresponds to the flattest design of the nozzle outlet (cf. Fig. 6).

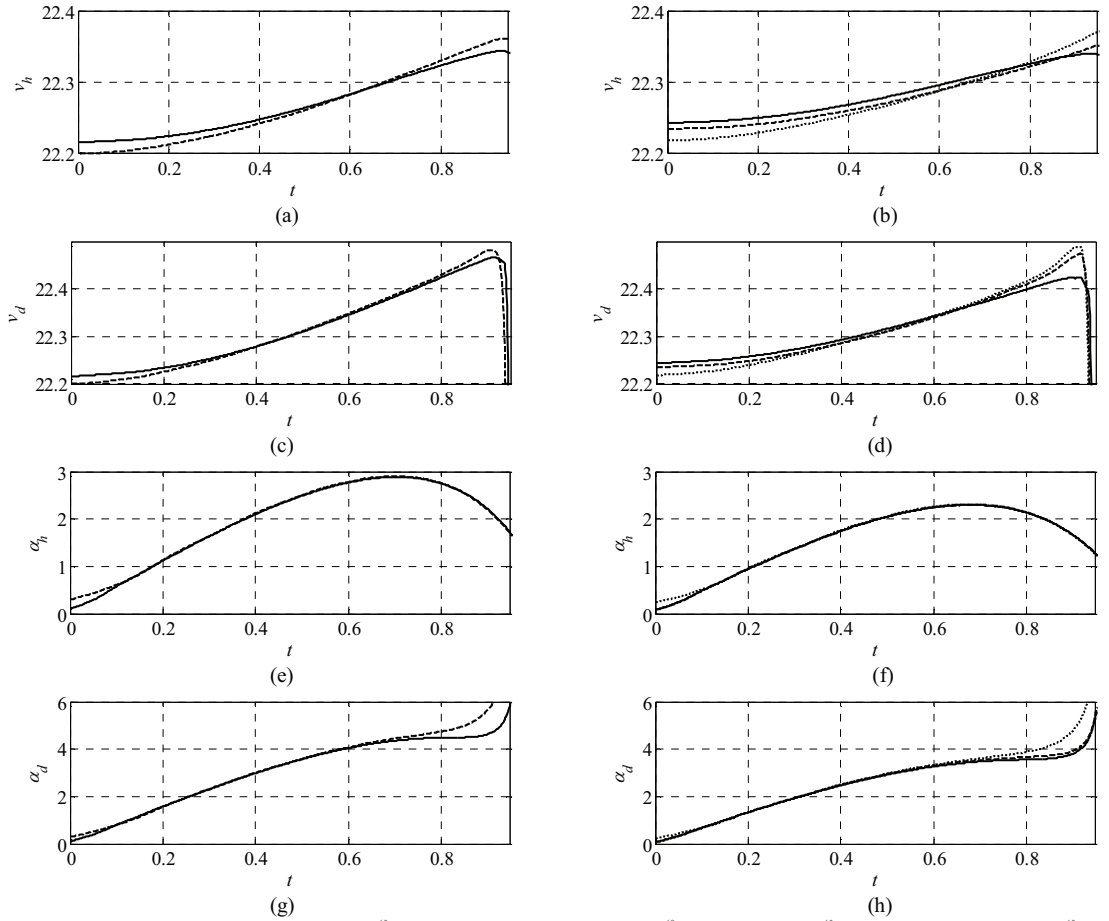

Fig. 4. High-, low-fidelity and surrogate models at $\boldsymbol{x}^{(i)}$ and at another design $\boldsymbol{x}$: (a) $v_{h.c}(\boldsymbol{x}^{(i)},t)$ (- - -) and $v_{h.f}(\boldsymbol{x}^{(i)},t)$ (—); (b) $v_{h.c}(\boldsymbol{x},t)$ (· · ·), $v_{h.s}{}^{(i)}(\boldsymbol{x},t)$ (- - -) and $v_{h.f}(\boldsymbol{x},t)$ (—); (c) $v_{d.c}(\boldsymbol{x}^{(i)},t)$ (- - -) and $v_{d.f}(\boldsymbol{x}^{(i)},t)$ (—); (b) $v_{d.c}(\boldsymbol{x},t)$ (· · ·), $v_{d.s}{}^{(i)}(\boldsymbol{x},t)$ (- - -) and $v_{d.f}(\boldsymbol{x},t)$ (—); (d)-(h) – analogous plots for the velocity angle.

3. Experimental Validation

In this section, we describe the measurements conducted in the wind tunnel after fabrication. In particular, we present measurements of the flow speed uniformity and fluctuating levels in the experimental test section.

3.1. Wind Tunnel Description

The low-speed wind tunnel is of open suction type and is composed of a square inlet with turbulence screens, settling chamber, contraction, test section housing, diffuser, and an axial fan (Fig. 6a). The inlet has a cross-sectional area of 2 m by 2 m. There are 3 turbulence screens, spaced apart by 100 mm, to break up any coherent large scale motions. The mesh density gradually increases from 12 per inch, then 16 per inch, and lastly 33 per inch. The settling chamber is 1.5 m long and allows for any small scale organized motions generated by the flow conditioning section to decay. The square contraction follows the settling chamber. The contraction is 2 m long with an area ratio of 8 to 1 that results in a 71 cm square entrance to the test section. The contraction contour was numerically optimized as described in the previous section (cf. Case 4 in Section 2.4). The inlet, settling chamber and contraction are all made from sheet metal. The enclosure surrounding the open jet test section has a volume of 13.5 m^3 and an axial length of 1.8 m. At the downstream end of the test section there is 80 cm square opening to the diffuser section. The diffuser section, made from sheet metal, transitions from a square cross-section to a 1 m diameter circle over a 2 m axial distance. The axial fan was manufactured by Fläkt-Woods and is driven by an 18 kW motor which is controlled by a variable frequency drive inverter. The maximum volumetric flow rate of the fan is 50,000 m^3/h; yielding a maximum flow speed of approximately 30 m/s in the test section.

Table 1. Wind tunnel contraction shape design: numerical results

Variable	Initial	Case 1[#]	Case 2[$]	Case 3[%]	Case 4[&]
x_1	0.25	0.3333	0.5000	0.3925	0.4977
x_2	0.50	0.6333	0.5038	0.6236	0.6840
x_3	0.70	0.6667	0.5556	0.5545	0.2691
x_4	0.70	0.6327	0.5025	0.5262	0.5305
$\Delta\alpha$ [deg]	4.62	3.8	1.6	2.0	0.7
Δv [%]	1.1	1.0	1.0	1.0	1.2
N_f	N/A	0	134	9	4
N_c	N/A	120	0	900	400
Total cost[*]	N/A	< 0.5	134	< 13	< 6

[#] Design obtained by direct low-fidelity model optimization using the pattern-search algorithm [12].

[$] Design obtained by direct high-fidelity model optimization using the pattern-search algorithm [12].

[%] Design obtained by SBO with trust region; surrogate model optimization performed using the pattern-search algorithm [12].

[&] Same as Case 3, but without the trust region framework.

[*] The total optimization cost is expressed in terms of the equivalent number of high-fidelity model evaluations. The ratio of the high-fidelity model evaluation time to the corrected low-fidelity model evaluation time is around 250.

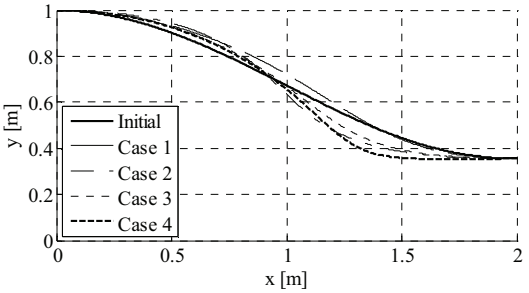

Fig. 5. Optimized nozzle shape obtained using four different design approaches: initial shape (—), the shape resulting from direct optimization of the low-fidelity model (– – –), the shape resulting from the direct optimization of the high-fidelity model (– · – ·), the shape obtained by surrogate-based optimization within trust-region framework (· · · ·), the shape obtained by surrogate-based optimization (no trust region) (- - - -).

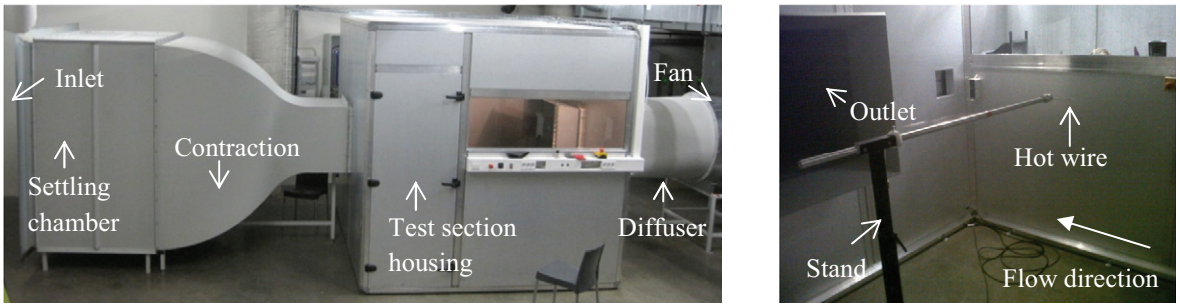

(a) (b)

Fig. 6. (a) A side view of the low-speed wind tunnel showing (from the left) the inlet (includes the bell mouth and turbulence screens), settling chamber, contraction, experimental section, diffuser, and axial fan. The overall length is 8 m. (b) A view inside the test section housing showing the single-component constant-temperature hot-wire probe on a stand.

3.2. Experimental Setup and Calibration

A single-component constant-temperature hot-wire anemometer system was used to investigate the flow uniformity, as well as the flow speed fluctuating levels, in the test section. The sensing element of the hot-wire probe was made from tungsten and had a diameter of 5 microns and length of nominally 1.2 mm. The sensing element was connected to the MiniCTA bridge. The output of the bridge was then digitized with a National Instruments data acquisition card with a 16-bit resolution. The sampling time was 6.5 seconds at 10 kHz. For the low order statistics presented here, we estimate the uncertainty in the hot-wire measurements to be less than 1%.

Calibration of the hot-wire probe was accomplished by placing a pitot-static probe in close proximity to the hot-wire and collecting data for a series of wind tunnel settings that extended over the full range of the VFD, i.e., from 0 to 50 Hz. For each of the free-stream velocity settings, mean values of both the hot-wire voltage and speed (calculated from the pitot-static probe) were determined, and a curve fit was used to relate the two. The error of the calibration curve fit of the mean velocities was less than 1% for all velocities.

In the test section, the hot-wire probe was placed on a stand facing the flow coming from the contraction exit as shown in Fig. 6b. By traversing the probe, measurements were taken in one cross-sectional plane, located 60 cm from the contraction exit, which is one third of the test section length. The measurements were taken at nine equally space locations, separated by 10 cm, in each direction, yielding a total of 81 measurements. The cross-sectional area where the measurements were taken was 80 cm by 80 cm and extended well outside the contraction exit area (71 cm by 71 cm).

3.3. Flow Uniformity and Fluctuation Levels

Contour maps of the mean velocity field and the turbulence intensity, calculated from the hot-wire probe measurements, are shown in Fig. 7 for three different free-stream velocity settings. The VFD was set to 10, 20, and 30 Hz, which yielded mean free-stream speeds of 5.4, 11.1, and 16.5 m/s (according to the calibration curve), respectively.

The mean velocity field contours indicate that the flow is uniform within the region of interest, the 85% area of the contraction exit, and the flow speed within the cross-section matches well with the free-stream velocity. However, there is a slight variation at the lowest free-stream velocity, where the speed is reduced to 5.3 m/s in the upper left hand corner (Fig. 7a). This variation of the flow speed is not within the measurement uncertainty. The authors believe that the reason for this variation is due to unsymmetrical inflow at the inlet caused by objects located in the experimental room located too closely to the upper left corner of the inlet. This will be rectified by clearing these objects.

The turbulence intensity contours indicate that the flow unsteadiness is rather high, ranging from 1 to 5% within the region of interest. A desired level of turbulence intensity is less than 1% in the whole cross-section. The turbulence intensity levels are controlled by the turbulence screens, with each new screen the level can be halved [20]. Currently, the wind tunnel has three turbulence screens; therefore, three additional screens are needed to reach the desired intensity levels.

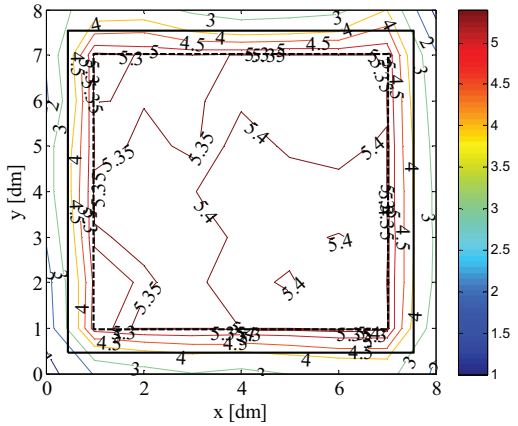

(a) Mean flow speed contours at $V_\infty = 5.4$ m/s

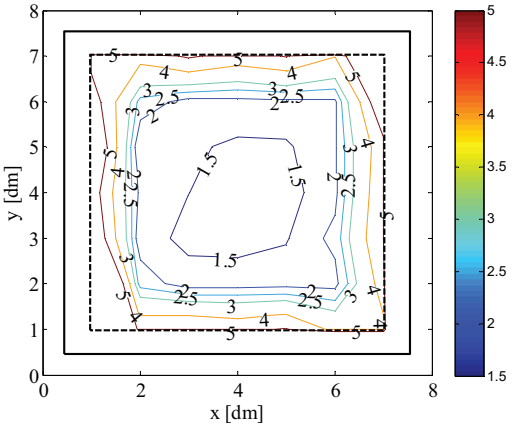

(b) Turbulence intensity contours at $V_\infty = 5.4$ m/s

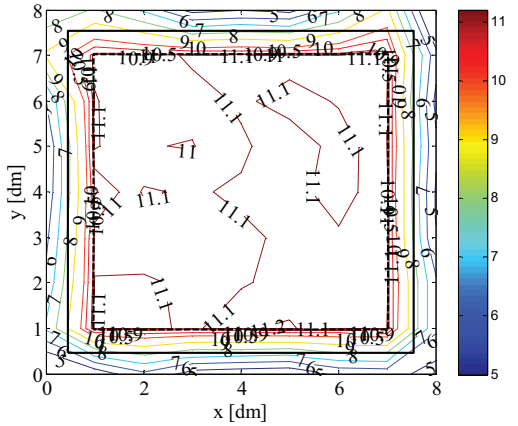

(c) Mean flow speed contours at $V_\infty = 11.1$ m/s

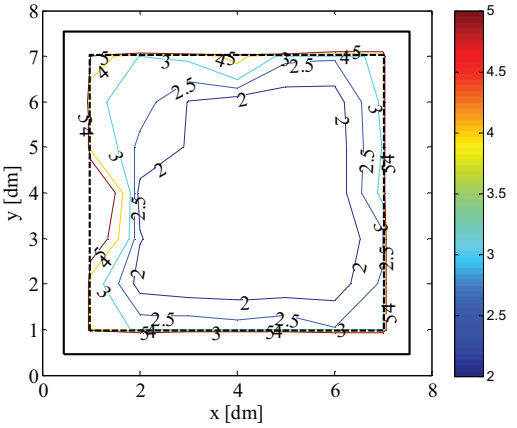

(d) Turbulence intensity contours at $V_\infty = 11.1$ m/s

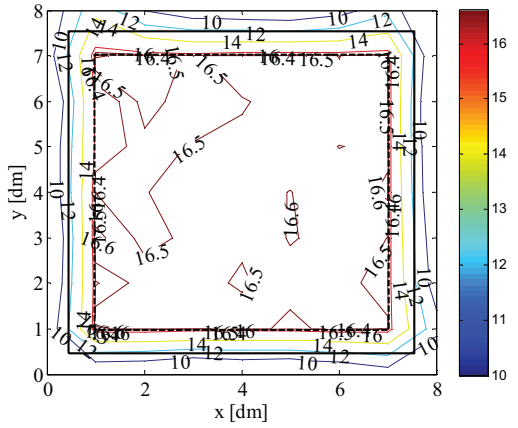

(e) Mean flow speed contours at $V_\infty = 16.5$ m/s

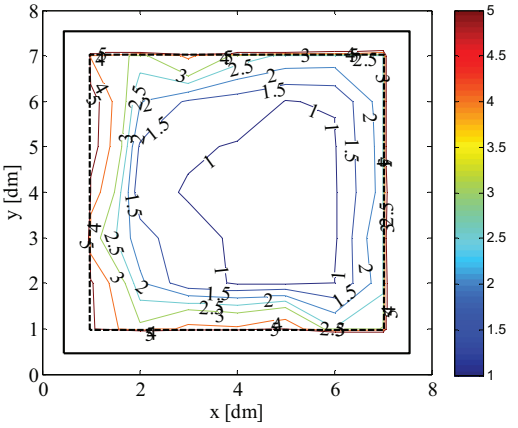

(f) Turbulence intensity contours at $V_\infty = 16.5$ m/s

Fig. 7. Flow uniformity and fluctuation levels at 33% of the test section length from the contraction exit. Data is shown for motor settings of 10, 20, and 30 Hz, or, mean free-stream speeds (V_∞) of 5.4, 11.1, and 16.5 m/s, respectively. Flow speed is given in m/s and turbulence intensity in %. The area of interest in the design optimization study (cf. Section 2) is shown here with the dashed lines (85% value of the contraction exit size). The contraction exit boundary is shown with solid lines.

4. Conclusions

We present an efficient design optimization of the wind tunnel contraction shape. The shape is parameterized using Bézier curves with five control points. The optimized design is obtained using surrogate-based optimization with the response-corrected low-fidelity CFD model exploited as a fast surrogate model that allows us to predict the optimum control parameters at a low computational cost. To our knowledge, it is the first application of SBO to wind tunnel contraction design. The design is verified through experimental measurements.

References

1. Barlow, J.B., Rae, W.H., and Pope, A., *Low-Speed Wind Tunnel Testing*, 3rd edition, John Wiley & Sons, 1999.
2. Watmuff, J., "Wind Tunnel Contraction Design," 9th Australasian Fluid Mechanics Conference, Auckland, New Zealand, Dec. 8-12, 1986.
3. Su, Y., "Flow Analysis and Design of Three-Dimensional Wind Tunnel Contractions," *AIAA Journal*, vol. 29, no. 11, 1991, pp. 1912-1920.
4. Doolan, C.J, and Morgans, R.C., "Numerical Evaluation and Optimization of Low Speed Wind Tunnel Contractions," *18th AIAA Computational Fluid Dynamics Conference*, Miami, Florida, June 25-28, 2007.
5. Mathew, J., Bahr, C., Carroll, B., Sheplak, M., and Cattafesta, L., "Design, Fabrication, and Characterization of an Anechoic Wind Tunnel Facility," *11th AIAA/CEAS Aeroacoustics Conference*, Monterey, California, May 23-25, 2005.
6. Lepine, J., Guibault, F., Trepanier, J.-Y., and Pepin, F., "Optimized Nonuniform Rational B-Spline Geometrical Representation for Aerodynamic Design of Wings," *AIAA Journal*, Vol. 39, No. 11, 2001, pp. 2033-2041.
7. Menter, F., "Two-Equation Eddy-Viscosity Turbulence Models for Engineering Applications," *AIAA Journal*, vol.32, 1994, pp.1598–1605.
8. ICEM CFD, ver. 12.1, ANSYS Inc., Southpointe, 275 Technology Drive, Canonsburg, PA 15317, 2006.
9. FLUENT, ver. 12.1, ANSYS Inc., Southpointe, 275 Technology Drive, Canonsburg, PA 15317, 2006.
10. Bandler, J.W., Cheng, Q.S., Dakroury, S.A., Mohamed, A.S., Bakr, M.H., Madsen, K., and Søndergaard, J., 2004, Space Mapping: The State of The Art. *IEEE Trans. Microwave Theory Tech.*, 52(1), pp. 337-361.
11. Queipo, N.V., Haftka, R.T., Shyy, W., Goel, T., Vaidynathan, R., and Tucker, P.K., 2005, Surrogate-Based Analysis and Optimization. *Progress in Aerospace Sciences*, 41(1), pp. 1-28.
12. Koziel, S., "Multi-fidelity multi-grid design optimization of planar microwave structures with Sonnet," *International Review of Progress in Applied Computational Electromagnetics*, Tampere, Finland, April 26-29, 2010, pp. 719-724.
13. Simpson, T.W., Peplinski, J., Koch, P.N., Allen, J.K., 2001, Metamodels for computer-based engineering design: survey and recommendations. Engineering with Computers. 17, pp. 129-150.
14. Koziel, S., and Bandler, J.W., 2010a, Recent advances in space-mapping-based modeling of microwave devices. *International Journal of Numerical Modelling*, (23) 6, pp. 425-446.
15. Søndergaard, J., 2003, Optimization using surrogate models – by the space mapping technique. Ph.D. Thesis, Informatics and Mathematical Modelling, Technical University of Denmark, Lyngby.
16. Echeverría, D., and Hemker, P.W., 2008, Manifold mapping: a two-level optimization technique. *Computing and Visualization in Science*. 11, pp. 193-206.
17. Koziel, S., 2010b, Shape-preserving response prediction for microwave design optimization. *IEEE Trans. Microwave Theory and Tech.*, 58(11), pp. 2829-2837.
18. Alexandrov, N.M., Lewis, R.M., 2001, An overview of first-order model management for engineering optimization. *Optimization and Engineering*. 2, 413-430.
19. Conn, A.R., Gould, N.I.M., and Toint, P.L., *Trust Region Methods*, MPS-SIAM Series on Optimization, 2000.
20. Barlow, J., Rae, W., and Pope, A., *Low Speed Wind Tunnel Testin*, John Wiley and Sons, 1999.